Design of monopiles for offshore and nearshore wind turbines in seismically liquefiable soils: Methodology and validation

Sadra Amani [a], Athul Prabhakaran [b], Subhamoy Bhattacharya [a,*]

[a] *Department of Civil and Environmental Engineering, University of Surrey, Guildford, GU2 7XH, United Kingdom*
[b] *Department of Structural Engineering, University of California, San Diego La Jolla, CA, 92093, USA*

ARTICLE INFO

ABSTRACT

An increasing number of offshore wind farms are being constructed in seismic regions over liquefaction susceptible soils. This paper presents a methodology for the analysis and design of monopiles in seismically liquefiable soils by extending the established "10-step methodology" with an additional 7 steps. These additional steps include assimilation of seismic data, site response analysis, stability check of the structure (ULS check through the concept of load-utilization ratio), input motion selection, prediction of permanent tilt/rotation, and ground settlement post liquefaction. A flow chart, which shows the interdependence of the different disciplines, is presented and can be extended to routine design. This proposed method is validated using the observed performance of an offshore and nearshore turbine from the Kamisu wind farm during the 2011 Great East Japan earthquake. Predicted results based on the proposed methodology compare well with the field observation and demarcate the (i) good overall performance of the offshore turbines and (ii) limit state exceedance of the nearshore turbine. It is envisaged that the proposed method will be useful towards the design of monopiles-supported wind turbines in seismic areas.

1. Introduction

Towards the end of 2020, the global wind energy generation capacity amounted to 733 GW, with new installations accounting for 111 GW, almost doubling that of 2019 [1]. Due to higher efficiencies and more stable wind conditions offshore than onshore sites, an increasing proportion of wind power is produced through large offshore wind farms. This demand for cost-efficient wind energy production has facilitated the industry to develop larger turbines with higher capacities. Fig. 1 presents the evolution of turbine capacity over the last 16 years, color-coded with rotor diameter. However, due to the high capital investments involved, profitability of these wind farms requires continuous operation and immediate functionality post-natural hazards. Therefore, the seismic resilience of OWTs is an important consideration in their engineering design and is, therefore, an area of active research. Readers are referred to recent publications [2–9] on various aspects of seismic design.

Water depth and ground conditions typically govern the choice of the OWT foundation system. Bottom fixed foundations are typically deployed in water depths up to 60 m. For depths up to 30 m, monopiles are preferred. Typical foundation systems between 30 and 60 m include monopiles, suction caissons, and jacket structures [11].

As translational and rotational inertia is largely concentrated at the top of OWTs, dynamic wind/wave loads can generate substantial moment demands on the foundations. Further, due to the sensitivity in the dynamic response of OWTs to changes in their natural frequency, soil and foundation flexibility need to be accounted for in the design stage. Seismic design of offshore wind turbine (OWT) foundations typically considers self-weight, wind, wave, 1P (rotor frequency), 3P (blade passing frequency), and seismic loads [11]. Fig. 2 shows the different load types applied to a turbine structure. The time scales for wind, wave, and seismic loads add further complexity to dynamics of OWTs. For example, cyclic wind loads have a period of around 100 s, whereas wave loads have a period of 10 s. Readers are referred to Arany et al. [12] and Bhattacharya [11] for further details.

Under seismic excitation, deep foundations experience demands due to *(i)* their inability to match free-field deformation (kinematic response) and *(ii)* inertia arising from superstructure (inertial response). Appraisal of these interactions is a necessary step towards the design of deep foundations for OWTs [15,16].

This paper introduces a methodology towards the seismic design of

Nomenclature and symbols:

		r_u	Excess pore water pressure ratio
OWT	Offshore wind turbine	R/A	(Resistance/Action) which is load utilization ratio
1P	Rotor frequency	ρ	Mass density
3P	Blade passing frequency	G_r	Low Strain Shear Modulus
H	Lateral load	$\varphi_{Triaxial}$	Triaxial friction angle
M	Induced Moment	φ_{PT}	Phase transformation angle
M_P	Plastic Moment	n	Pressure dependence coefficient
ULS	Ultimate Limit State	γ_{max}	Maximum Shear Strain
SSI	Soil-Structure-Interaction	p'_r	Reference mean confinement
UHS	Uniform Hazard Spectra	CSR	Cyclic Stress Ratio
SLS	Serviceability Limit State	$N_{1,60}$	Corrected SPT blow count
FLS	Fatigue Limit State	PGA	Peak Ground Acceleration
DLC	Design Load Case	NS	North-South direction
RNA	Rotor Nacelle Assembly	EW	East-West direction
UDL	Uniformly Distributed Load	API	American Petroleum Institute
PIMY	Pressure Independent Multi-Yield model	GEER	Geotechnical Extreme Events Reconnaissance
PDMY02	Pressure Dependent Multi Yield 02	NIED	National Research Institute for Earth Science and Delivery Prevention
ξ	Damping ratio		
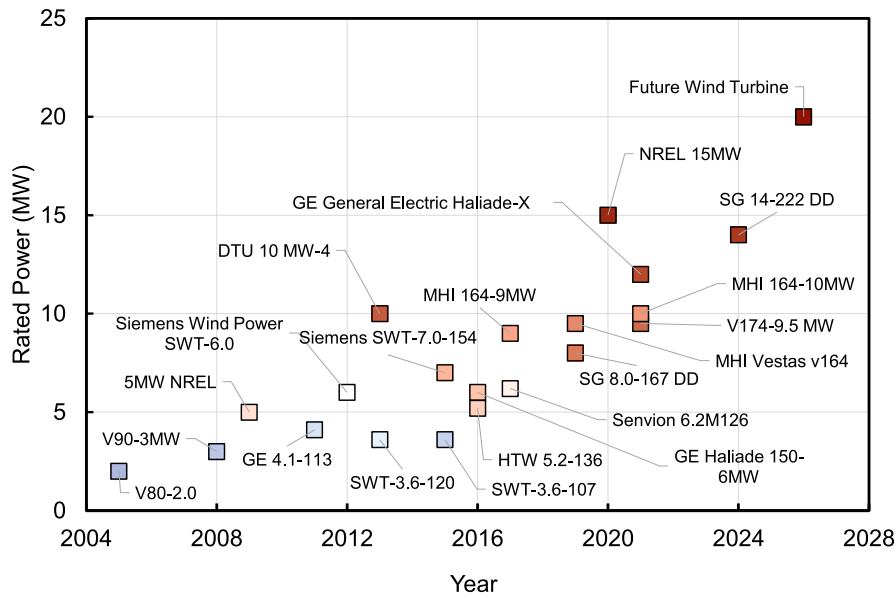
Fig. 1. Evolution of turbine capacity over the last 16 years [10]. The data represents the Turbine make, capacity, and blade diameter.

monopile-supported OWTs accounting for kinematic and inertial effects. In the following section, the methodology is presented, with considerations to ground motion selection, site response analysis, and dynamic soil-structure interaction. Further, a case study is presented to validate the methodology based on observed response to a set of turbines from Japan during the 2011 Great East Japan (Tohoku) earthquake.

2. Methodology for the seismic design of nearshore and offshore wind turbines

This section presents a methodology to design nearshore and offshore wind turbines in seismic regions. Typical limit states for OWT design include an ultimate limit state (ULS), serviceability limit state (SLS), and fatigue limit state (FLS) criteria. ULS criteria are necessary to ensure that the structure and foundation remain safe and exhibit minimal plastic deformations during extreme loading. SLS criteria are necessary to ensure that the pile head tilt, rotation, and RNA acceleration is within an acceptable range. Finally, FLS criteria are necessary to appraise the long-term life of the structure (*e.g.*, high cycle fatigue loading, seismic events, *etc.*). Limit states considered for seismic design are discussed below:

(i) Seismic considerations-ULS: The presence of liquefaction/strain-softening susceptible layers in the soil can reduce the ultimate
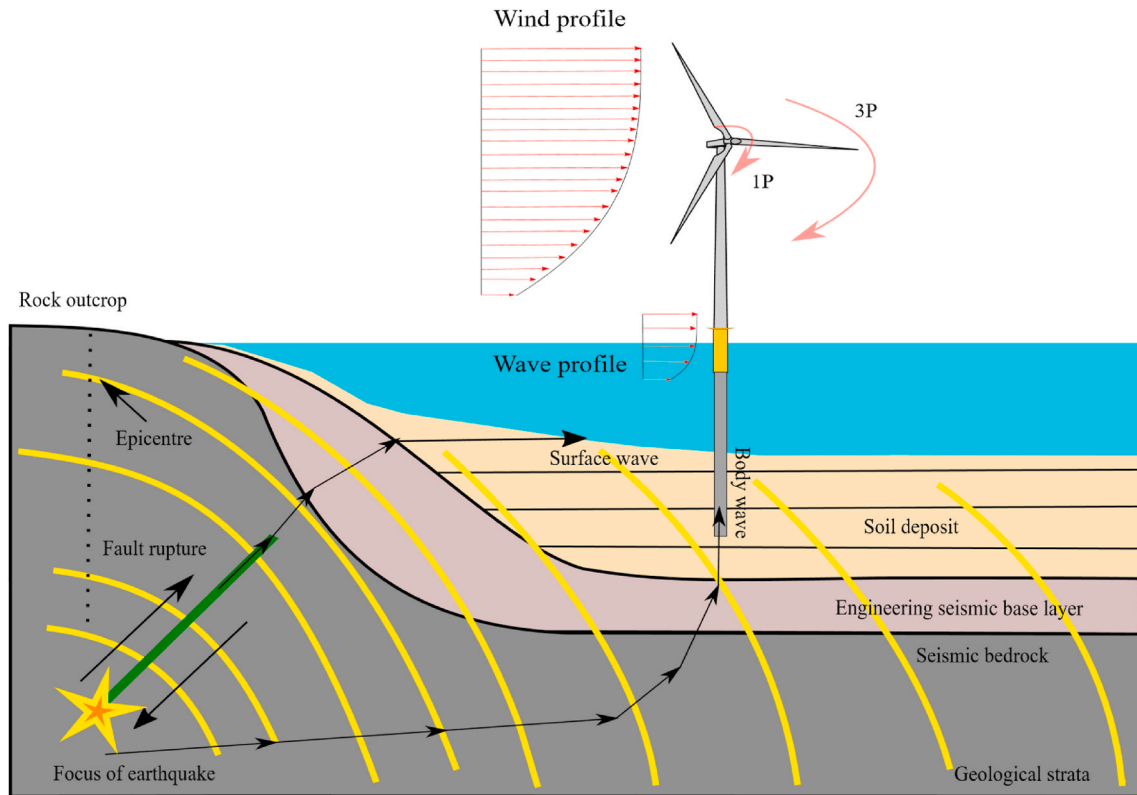
Fig. 2. General loading configuration of offshore wind farms in seismic regions [13,14].

capacity of embedded foundations. Further, under static shear stresses, ground failure can lead to the mobilization of large soil masses and increased demands on the foundation system.

(ii) Seismic consideration-SLS: Strong shaking can increase demands on the rotor-nacelle assembly (RNA), permanent tilt/deformation at the pile head.

(iii) Seismic consideration-FLS: The large number of cycles imposed by wind/wave load can induce high cycle fatigue. This condition must be accounted for the seismic design of OWTs, where the capacity of the foundation system must be reduced to account for the fatigue load. It is noted that OWTs incur a much larger number of cycles during storm and typhoon loading compared to earthquake loads. However, seismic loads can incur large shear strains to the soil deposit. Therefore, considerations should be made towards changes to the fatigue life of the turbine, particularly post-seismic events.

A summary of typical limit states in OWT deep foundation design is detailed in Table 1. Readers are referred to Bhattacharya [11] for further details.

Table 1
ULS, SLS, and FLS criteria.

Limit State	Typical criteria
ULS	(i) Ground Failure (soil failure) causing foundation collapse
	(ii) Foundation should remain elastic
SLS	(i) Permanent tilt at pile head <0.5–0.75 deg (these are typical for grounded systems)
	(ii) RNA acceleration <0.2–0.4 g
	(iii) Acceptable pile head deformation
FLS	(i) Wind + Wave loading imposes many cycles during the operational life of the turbines
	(ii) Fatigue life needs to be quantified after a seismic event

Once the limit states at each hazard level are explicitly defined, the proposed methodology (outlined in Fig. 3) can be used to obtain a preliminary foundation design. These steps outlined in Fig. 3 are as below:

1. Input Data Assimilation:

Prior to analyses, information regarding the turbine, site, and hazards need to be obtained, including

(i) *performance requirement (limit states)* includes ultimate limit state (ULS), serviceability limit state (SLS), and fatigue limit state (FLS) checks. The readers are referred to Table 1 for further details on the performance requirements.

(ii) *turbine data* includes wind turbine specifications such as blade diameter, rotor, blade passing frequency (1P, 3P), tower specifications (height, thickness, diameter).

(iii) *metocean data* could be collected from metrological stations nearby the site. These data could be wind speed (operational, turbulent), wave height, and period.

(iv) *site characterization* study is required to investigate the soil properties, soil layers, types, and water depth.

(v) *seismic and tsunami hazard analyses* should be conducted for seismic regions for different return periods.

2. Preliminary design: For the estimation of the pile dimensions, this step must be fulfilled. The preliminary design methodology could be carried out using the 10-step method presented in Arany et al. [12].

3. Identification of layers that can rapidly lose strength and stiffness during earthquake loading using liquefaction triggering analysis (only in seismic regions).

4. Site response analysis: Appropriate soil constitutive models should be used to obtain soil displacement histories along the length of the
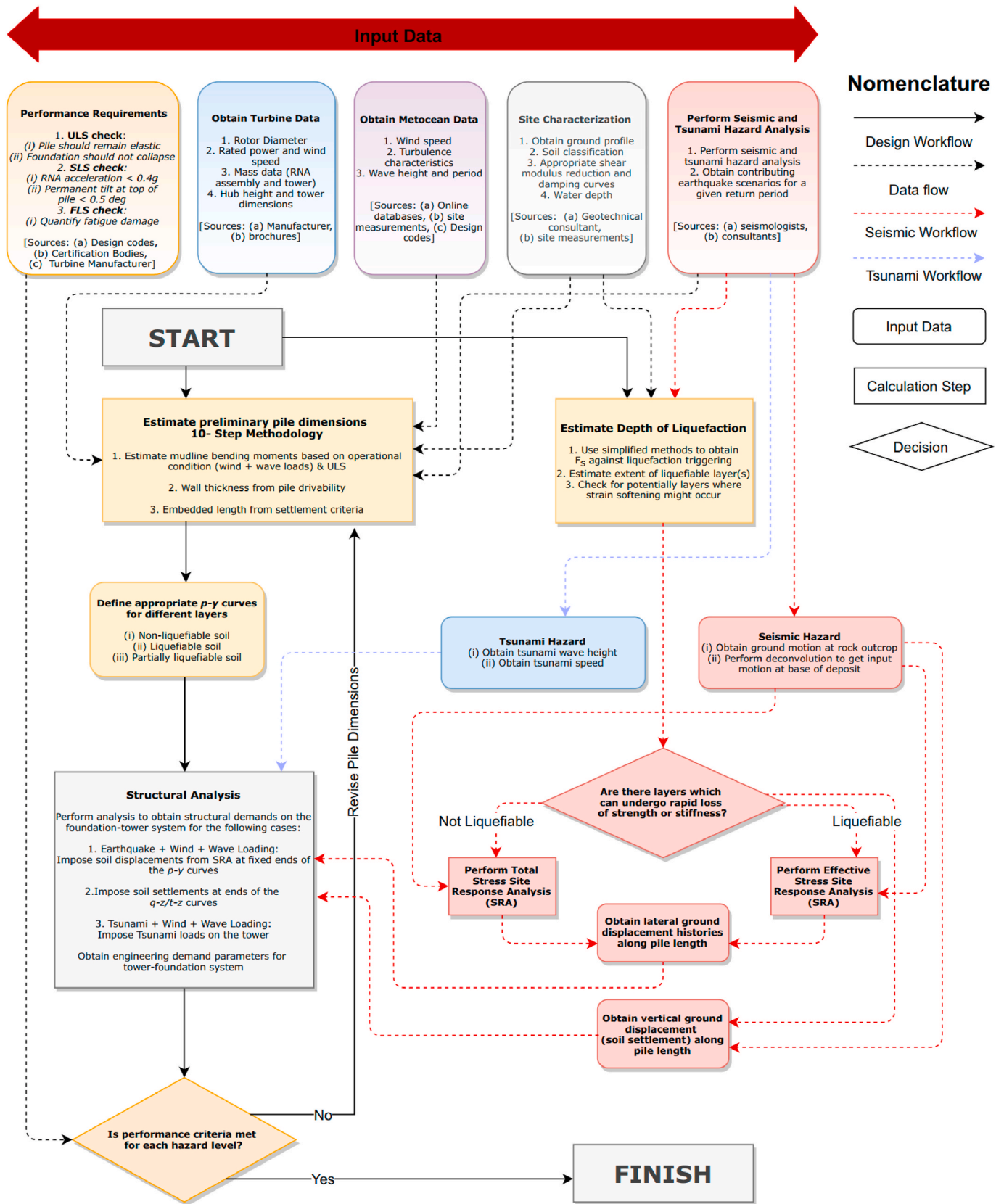
Fig. 3. Workflow for monopile design for wind turbines in seismic zones.

pile. The user can perform a total/effective stress analysis based on the soil profile and expected level of shaking.

5. Definition of appropriate *p-y* curves for soil layers precluding and including strength loss (in the event of soil liquefaction/cyclic softening).
6. Structural modeling of the tower-monopile system using appropriate structural properties. Imposition of wind, wave, and tsunami load (if applicable) on the tower structure.
7. Imposition of soil displacement histories obtained from step (4) to the fixed end of the soil spring.
8. Dynamic foundation-structure interaction analysis.

2.1. Ground motion selection

In design practice, the seismic hazard at a site is described in terms of a Uniform Hazard Spectra (UHS), obtained from a probabilistic seismic hazard analysis. However, selecting hazard consistent ground motions using a UHS has proven to provide conservative estimates of structural response as the UHS is not defined through a single earthquake scenario. More appropriately, the Conditional Mean Spectrum [17] and Generalized conditional mean spectrum [18] can be used to obtain the suite of ground motions at the rock outcrop. A detailed review of possible ground motion selection methodologies could be found in Katsanos et al. [19].

The UHS is commonly prepared for rock outcrop sites. The methods discussed above could be utilized to obtain a suite of hazard consistent ground motions (at the rock outcrop). Once the rock outcrop motion is obtained, deconvolution can be used to obtain the ground motion at bedrock [20]. The suite of ground motions developed for bedrock is the input to the site response analysis.

2.2. Site response analysis

The free-field response of the ground (away from the deep foundation) to the suite of ground motion developed at the bedrock level can be obtained through a site response analysis. If assumptions for 1D wave propagation hold [21], the shear stress-strain response of soil layers can be characterized through appropriate shear modulus reduction and damping curves. Based on project requirements, these curves can be site-specific or generic, based on the client's requirements. This approach would constitute a total stress-based site response analysis. Pore pressure, soil dilation, *etc.*, can be incorporated using an effective stress-based approach with appropriate constitutive models. It is noted that equivalent linear analyses are usually performed in the frequency domain and cannot account for soil softening due to pore-pressure development [22]. Therefore, analysis of a deposit with liquefaction susceptible layers would require an appropriate soil constitutive model.

Displacement demands from the ground are then imposed on the pile through an appropriate set of load-deformation curves (*p-y*). It is noted that ground response analysis can account for the development of shear strain contrasts (based on the soil profile) and associated kinematic demands.

2.3. Soil-structure interaction

The free-field response of the soil deposit is connected to the response of deep foundations through appropriate *p-y* curves. This
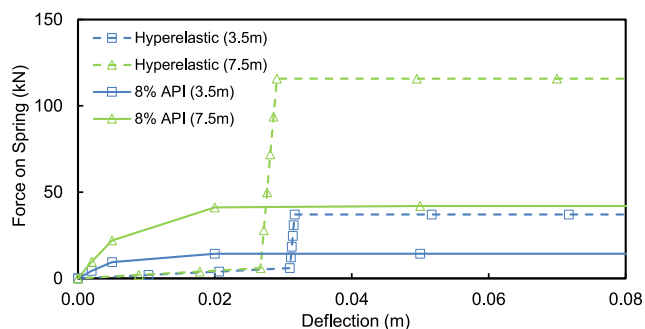
Fig. 4. Typical hyperelastic and reduced API *p-y* curves.

method treats the pile as a beam on a nonlinear Winkler foundation (BNWF), where pile-soil interaction is modeled using discrete nonlinear *p-y* springs.

It is critical to note that *p-y* curves employed in practice are often mechanism/hazard-specific. Therefore, considerations towards appropriate mechanisms should be accounted for in the selection of relevant *p-y* curves. For example, in strain-softening/liquefaction susceptible deposits, appropriate modifications can be made to the *p-y* curves to represent strength/stiffness loss. Several techniques currently exist in literature to model the *p-y* curve for liquefied soil, including *p* multiplier reduced *p-y* curves [23], hybrid curves [24], and zero strength *p-y* curves [25]. Further after onset of liquefaction, effects of soil dilation can be accounted for using strain hardening *p-y* curves as mentioned in Lombardi et al. [26] or Dash et al. [27]. Therefore, the selection of inappropriate *p-y* springs could lead to overestimation or underestimation in design based on the problem analyzed. Typical *p-y* springs for liquefied soil using the *p* multiplier (8%) reduced API and hyperelastic formulations are shown below in Fig. 4.

Fig. 5 describes the schematic concept of the soil-structure interaction (SSI) model using *p-y* springs.

2.4. Identification of liquefiable or strain softening layers

If layers are susceptible to soil liquefaction, simplified methods such as Idriss and Boulanger [28], Robertson and Wride [29], Kayen et al. [30], and Seed et al. [31] can be used to estimate the likelihood of triggering (check for initial liquefaction, *i.e.*, $r_u = 1$). However, sufficient strength loss can occur and lower r_u values, which must be considered from a design perspective. Further, simplified methods assume each layer acts independently, leading to challenges in stratified sites, as noted by Beyzaei et al. [32].

Determination of strain-softening layers can also be identified using the method presented by Idriss and Boulanger [28]. In addition, liquefaction triggering analysis is dependent on the hazard level considered (liquefaction might not trigger for low hazard levels, *e.g.,* design basis event, but might trigger for the maximum credible event).

2.5. Load utilization ratio analysis

The load utilization ratio of monopile can be used to obtain the demand/capacity ratio of a pile under combined lateral and flexural loading [33,34]. The utilization ratio can be easily depicted graphically (Fig. 6), where M_R and H_R represent the resistance capacity of a pile for the applied Moment (M) and Lateral load (H), which can be predicted
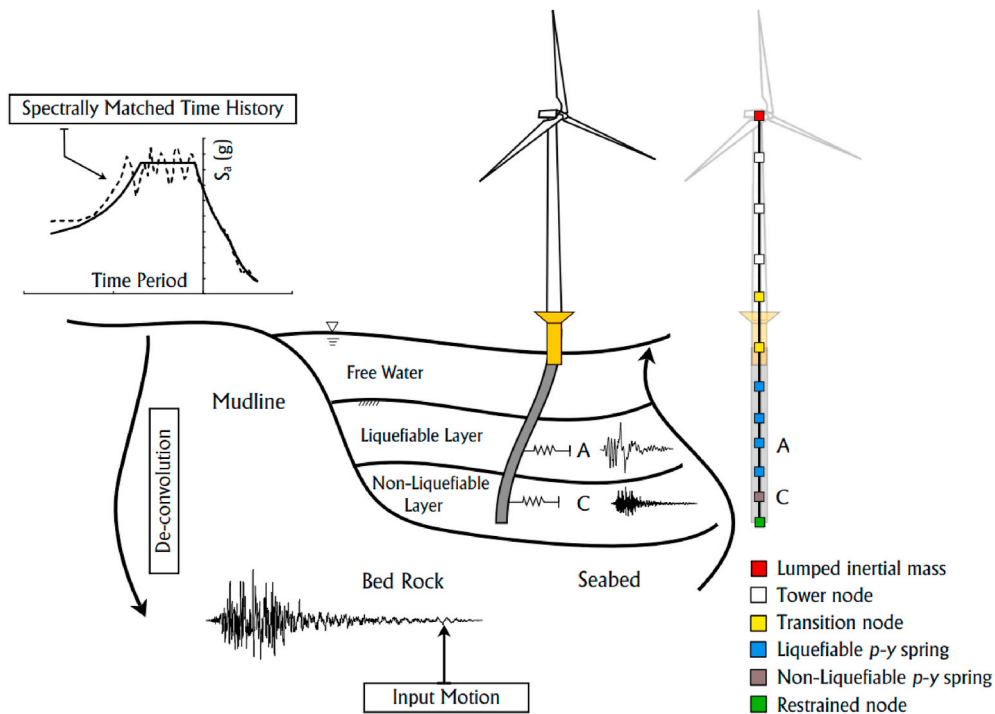
Fig. 5. Schematic concept of soil-structure interaction model (*p-y* spring).

using the *p-y* spring method. The epistemic uncertainty of using specified *p-y* curves can be treated using multiple constitutive models.

As shown in Fig. 6, the failure surface could vary based on the chosen soil constitutive model. Therefore, an idealized soil failure envelope line is defined. Then, knowing the distance of the design load case (DLC) point from the idealized line, the load utilization ratio *(R/A)* could be found.

Equation (1) is derived based on the provided geometry to calculate the ratio between the resistance (R) and load (A) to obtain the load utilization ratio.

$$FOS(A,B) = \frac{R}{A} = \frac{\sqrt{\frac{(H_i M_R H_R)^2 + (M_i M_R H_R)^2}{(M_i H_R + M_R H_i)^2}}}{\sqrt{M_i^2 + H_i^2}} \qquad \text{Equation 1}$$

2.6. Analysis of soil settlement post liquefaction

As a result of soil liquefaction, sand boil, land subsidence, or excessive settlement could be observed in the field [35]. Liquefaction-induced consolidation settlements in the free field can be reasonably predicted using Tokimatsu and Seed [36], Ishihara and Yoshimine [37], or Zhang et al. [38]. The parameters of this chart are based on CSR and the adjusted SPT N-value ($N_{1,60}$).
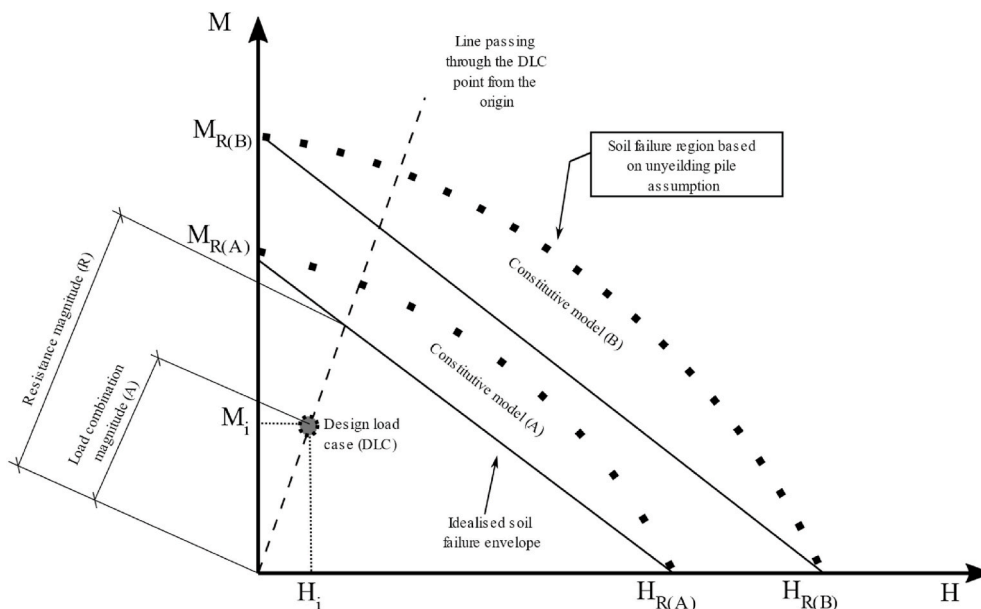
Fig. 6. Construction of the load utilization ratio.
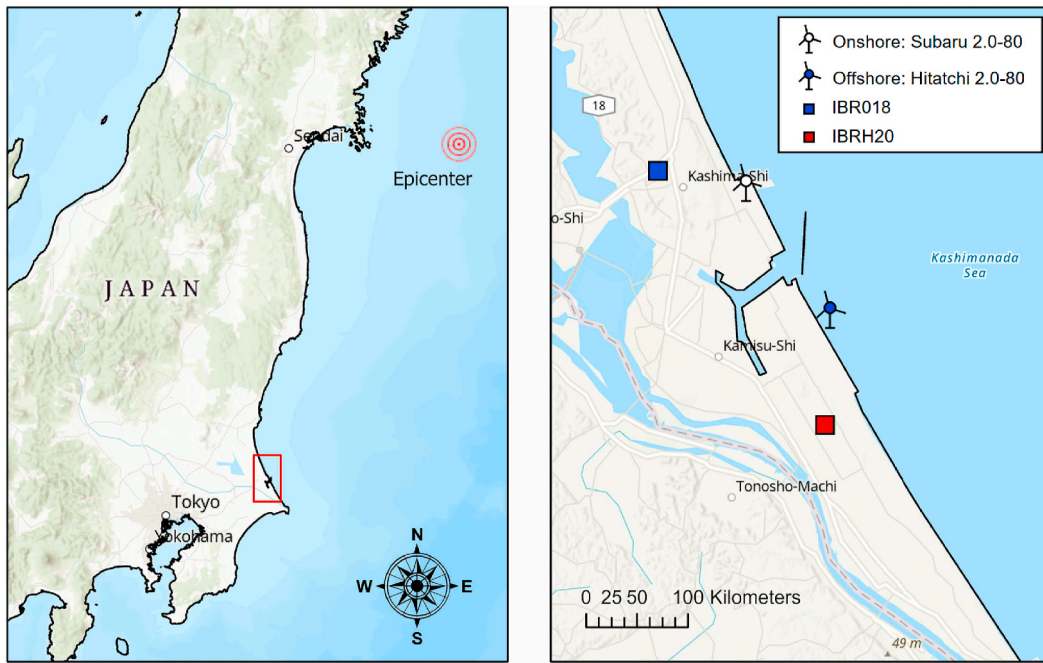
Fig. 7. Satellite view of Kamisu wind farm [48].

3. Validation using Kamisu wind farm

The performance of a Japanese wind farm during the 2011 9.0 M_w Great East Japan (Tohoku) earthquake is considered to validate the proposed methodology. To the authors' knowledge, 'Wind Power Kamisu' is the only farm containing turbines subjected to earthquake and tsunami loads. Further, reconnaissance surveys indicated extensive soil liquefaction in close proximity to the nearshore turbines [39–41].

Therefore, this case study presents a unique opportunity to verify current seismic design practices in pile-supported wind turbines.

Wind Power Kamisu [42] includes two main wind farms. One is located 50 m away from the shoreline (Kamisu nearshore wind farm-Phase 1), and the other is about 60 m away from the coast (Kamisu nearshore wind farm) at Kashima City in the Ibaraki prefecture [39]. Phase 1 of the Kamisu nearshore wind farm was commissioned in 2010 as Japan's first offshore wind farm. This wind farm included 7 Hitachi

(i) Offshore turbines

(ii) Nearshore turbines

Fig. 8. (i) Street view of Kamisu offshore wind farm [49], (ii) Street view of Kamisu nearshore wind farm [39].

HTC-2.0-80 turbines with a rated capacity of 2 MW to provide a total output of 14 MW on the offshore zone. These wind turbines were installed on monopiles, which extended 17 m below the seabed. The preliminary design of the offshore turbines can be found in Matsunobu et al. [42]. The Kamisu nearshore wind farm was commissioned in 2006 near the Kashima port prior to its offshore counterpart. The nearshore wind farm consists of Subaru 2.0–80 wind turbines, supported on pile groups extending 17 m into the soil. The satellite view and the street view of Kamisu wind farm are shown in Fig. 7 and Fig. 8.

During March 11, 2011, 9.1 M_w Great East Japan earthquake, nearby

(i)
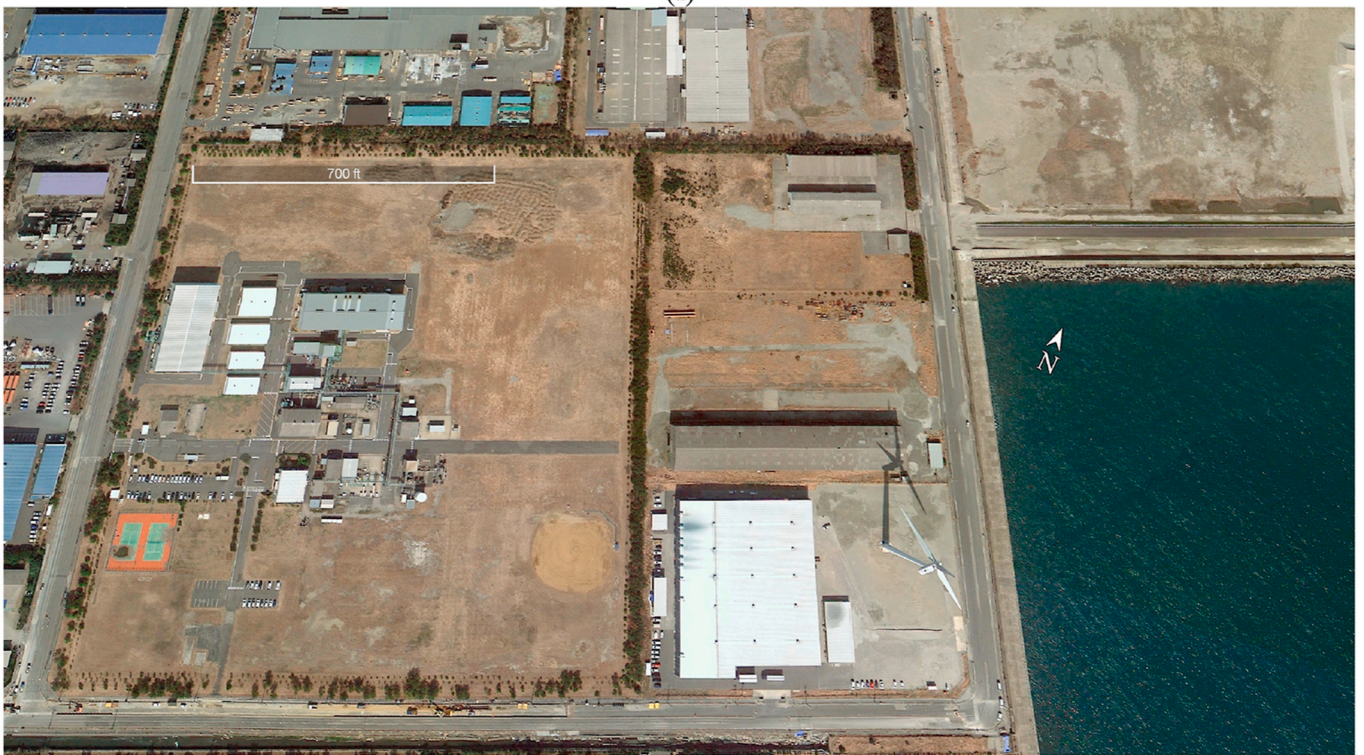
(ii)

Fig. 9. (i) Eighteen days after the earthquake (ii) One year after the earthquake [40]. Evidence of soil liquefaction can be observed through the manifestation of soil ejecta in part (i).

Kashima city (station IBR018, [43]) recorded a peak ground acceleration of about 0.65g at the ground surface. Strong shaking was followed by a tsunami which caused widespread destruction in different parts of Kamisu city [44]. During the Tohoku 2011 earthquake, the offshore wind turbines reported no mechanical failure. However, due to grid connection issues, wind turbines shut down for three days, and after that, the wind turbines resumed their operation [45–47].

Fig. 9 indicates the location of a nearshore wind turbine next to Kashima port. All but one of the nine turbines at this location performed well, having negligible residual tilt, despite strong shaking and soil liquefaction. Fig. 9 (i) presents evidence of soil liquefaction and ejecta in the region. A reconnaissance survey by GEER indicated that one turbine (presented in Figs. 9 and 10) had a residual tilt of about 1.6 deg. Cracks on the ground surface and soil settlement around the pile cap near the tilted turbine were found as presented in Fig. 10 (i) and (ii), respectively. The piles in the group for the nearshore turbines are seated on dense sand. Therefore, the settlement observed in Fig. 10 (ii) around the pile group [39].

Satellite photographs in Fig. 9 indicate a preferential manifestation of soil ejecta towards the northern part of the turbines. Near the tilted structure, several identical turbines experienced little to no tilt. Therefore, it is likely that local soil conditions (spatial variability) in the deposit played a significant role in the failure of the tilted turbine.

3.1. Soil profile and site response analysis

Strong motion data from the KiK-Net and K-Net stations [43] close to the wind farm were used to obtain the ground response during the 2011 Great East Japan earthquake. Soil surface motions from stations IBR018 (Kashima port) and IBRH20 (Hasaki-2) were selected for the nearshore and offshore turbines, respectively. The recorded motions and corresponding 5% damped response spectra recorded at the Kashima port and Hasaki-2 stations are presented in Fig. 11 and Fig. 12, respectively. Deconvolution was performed employing *DeepSoil* [50] to obtain the 'within' motions at a depth of 20 m for both deposits using the soil profiles provided in the KiK-Net database. Modulus reduction and damping curves suggested by Anbazhagan et al. [51] were employed.

Soil profiles from boreholes closer to the turbines were obtained from the NIED Geo-Station database [52] and used to perform the site response analysis using the 'within' motions obtained earlier. The soil profiles used are presented in Fig. 13 (i) and (ii), respectively. The groundwater table for the nearshore site was about 5 m below the soil surface.

The 'within' motions obtained were propagated through a 1D effective stress site response analysis performed in OpenSees [53] to obtain the free-field response of both deposits. In each deposit, liquefiable layers are modeled using the Pressure-Dependent Multi-Yield surface (PDMY02) constitutive model developed by Elgamal et al. [6] and Yang et al. [54]. The non-liquefiable soil is modeled using the Pressure Independent Multi-Yield model (PIMY) to prevent a reduction of strength with loss of confinement.

A modest stiffness proportional damping of 0.3% is considered in the site response analysis for numerical stability (the main source of damping arises from hysteretic response of the soil). Parameters used in the model are presented in Table 2. The motions were corrected for accelerometer orientation with the fore-aft and side to side directions of the turbines based on aerial photographs shown in Fig. 9.

Computed soil displacement time histories obtained from the site response analysis are presented in Fig. 14 and Fig. 15, respectively, for offshore and nearshore wind farms. The responses indicate the

(i) Cracks on ground surface near the tilted turbine indicative of liquefaction induced soil movement

(ii) Soil settlement around the pile cap of the tilted turbine

Fig. 10. (i) Nearshore Kamisu wind farm before the earthquake (ii) 18 days after the earthquake with the evidence of soil ejecta [39].

mobilization of ground displacements, particularly at depths of stiffness contrast, after the onset of soil liquefaction. The free-field response of the ground is then imposed to the far ends of the compatible *p-y* springs to obtain the demand on the monopile.

3.2. Loads cases considered in design

The offshore and nearshore turbines' tower-foundation system was subjected to both operational and extreme loads under SLS and ULS conditions. Therefore, OWTs should resist earthquake inertia and the loads imposed under SLS conditions. Table 3 and Table 4 summarize the load cases considered in the analysis of the offshore and nearshore wind farms, respectively.

Wind loads

Under operational conditions, the estimated mean wind speed at the site is about 7 m/s [55] for both sites. However, under different load
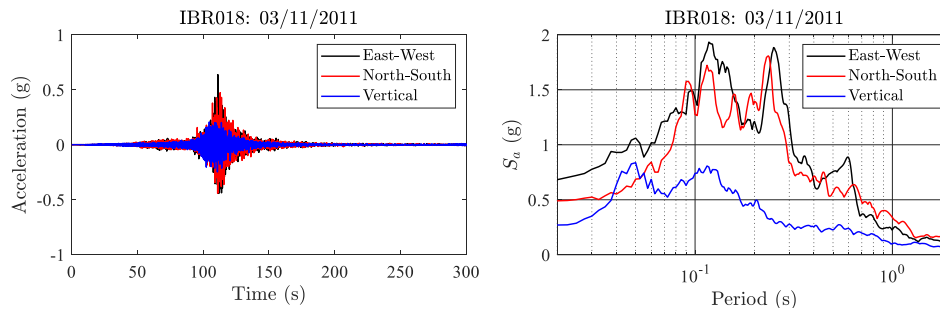
Fig. 11. Recorded motion on the soil surface and corresponding 5% damped response spectra at Kashima port (K-Net station: IBR018).
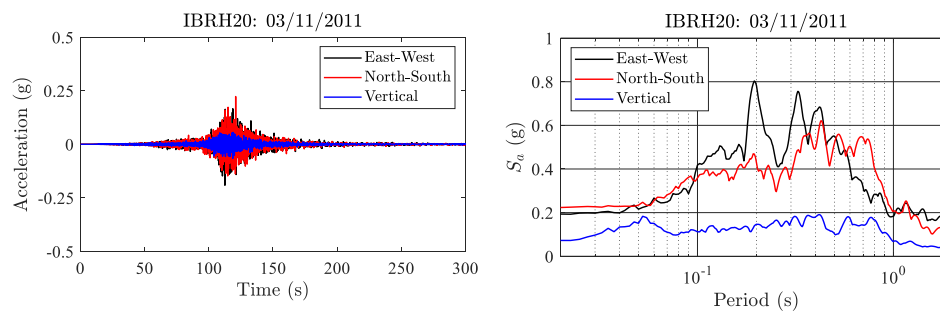
Fig. 12. Recorded motion on the soil surface and corresponding 5% damped response spectra at Hasaki-2 (KiK-Net Station: IBRH20).

cases, different wind load types are defined. These loads could be divided into three types:

Extreme wind loads

The maximum wind load that a wind turbine could experience. Matsunobu et al. [42] estimated this load as 985 KN; however, based on the obtained wind speed from Global Wind Atlas [55], the estimated extreme wind load by Matsunobu et al. [42] is validated using the method proposed by Arany et al. [12].

Operational wind loads

Describes the wind load during the operating condition similarly; this value is estimated by Matsunobu et al. [42] and validated using the method proposed by Arany et al. [12] as 293 KN.

Shut down loads (turned off condition)

Specified as a point load on the top of the tower during its Shut down period. This value was estimated using the method proposed by Arany et al. [12] as 190 KN.

Wave loads

A uniformly distributed load (UDL) estimated at 138 kN/m [42] was specified from the mudline level up to a height of 6.92 m for wave loading for the offshore site. The mean water depth at the Kashima-Nada Sea is about 4.5 m, with a period of about 13 s. The wave load distribution profile is presented in Fig. 16 (ii). No wave load is considered for the Kamisu nearshore wind farm as the water table is 4.82 m below the ground level.

Tsunami loads

Based on observations from Matsunobu et al. [42], the mean sea level and tsunami height at Kashima city during the Tohoku (2011) earthquake event was recorded at 4.5 m and 5.7 m, respectively. In this study,

only a tsunami run-up analysis was performed. It is assumed that the backwash provided similar demands on the tower. Therefore, a uniformly distributed load of 138 kN/m was specified across a run-up height of 5.7 m (10.2 m from the mudline level). In addition, for the Kamisu nearshore wind farm, the tsunami height was only considered as 5.0 m from the ground level. Therefore, the assigned UDL to tsunami load was 138 kN/m. The tsunami load distribution profile is illustrated in Fig. 16 (iii).

Earthquake loads

The free-field response of the ground is obtained from the site response analysis and is imposed on the far ends of compatible *p-y* curves for both offshore and nearshore turbines. The relative ground displacement was obtained from site response analysis, as shown in Fig. 15. The free-field response was obtained and assigned to the end of *p-y* springs based on two directions (Bi-directional). One direction represents the ground displacement in the north-south (NS) direction and the other east-west (EW).

3.3. Soil-structure interaction analysis

The offshore wind farm foundation system consists of a single pile embedded in the soil, extending up to 17 m below the seabed. The pile is modeled using linear elastic beam-column elements with a 3.5 m diameter pile section of 42 mm thickness. The nearshore wind turbines are supported by a pile group consisting of 12 piles of length 17 m and diameter of 0.8 with an octagonal pile cap [39]. The pile is modeled using linear elastic beam-column elements with a 0.8 m diameter pile section of 0.3 m thickness.

(i)

(ii)
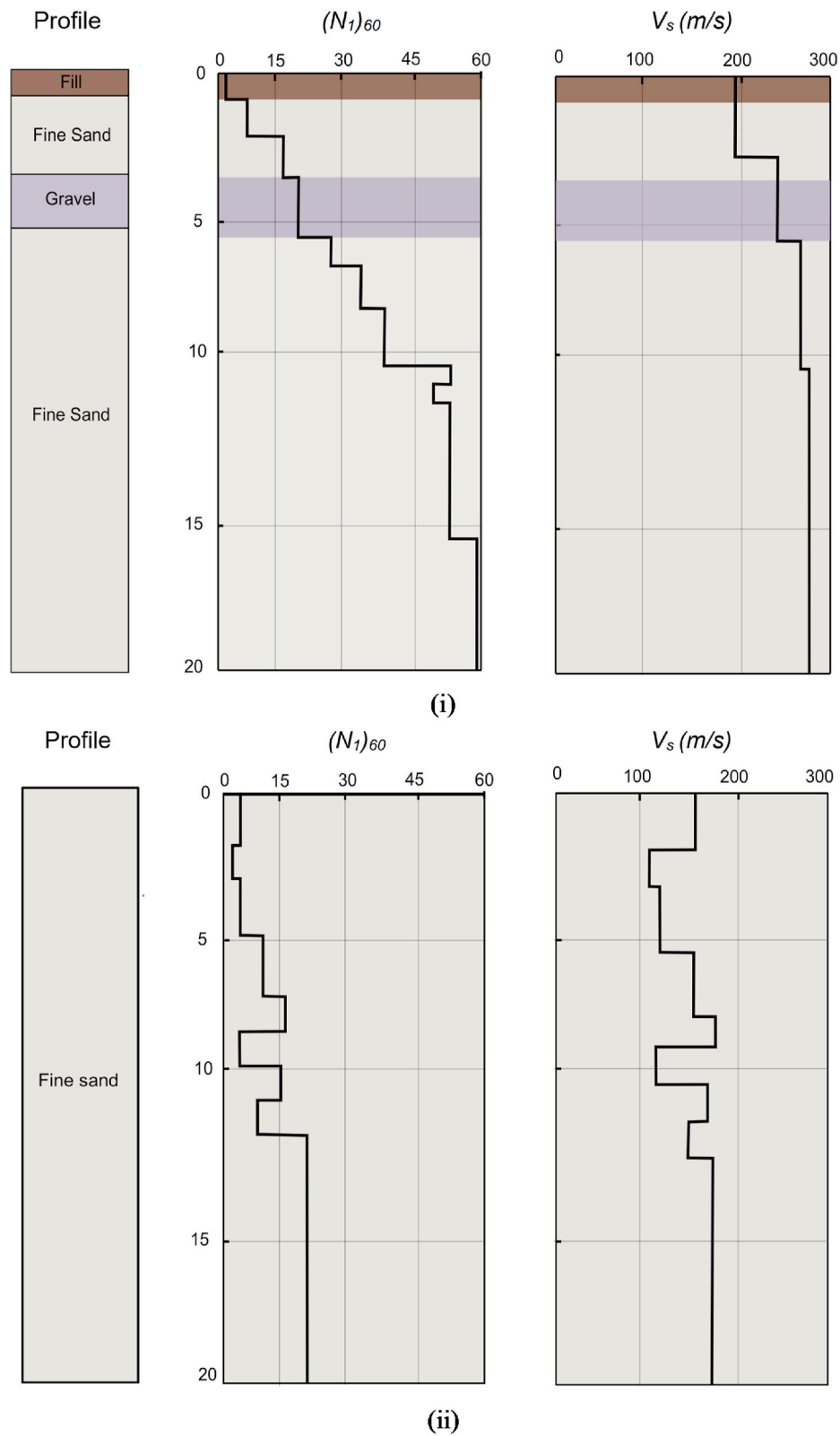
Fig. 13. (i) Ground profile at Kamisu offshore wind farm [43], (ii) Ground profile for the nearshore wind farm [52].

Table 2

Parameters used in the site response analysis for the offshore and nearshore wind farms [53].

Deposit	Offshore				Nearshore
Model Parameters	Fill	Fine Sand	Gravel	Fine Sand	Fine sand
Constitutive Model	PDMY02	PDMY02	PDMY02	PDMY02	PDMY02
$(N_1)_{60}$	3	11	20	40	10
Mass density, ρ (t/m^3)	1.6	1.8	2	2.05	1.8
Low Strain Shear Modulus G_r (MPa)	37	54	95	112	51
Poisson's ratio for dynamic analysis	0.33	0.33	0.33	0.33	0.33
Friction angle describing strength as $p'\sin(\varphi)$	28	29	34	38	33
Phase transformation angle (φ_{PT})	–	–	30	32	31
Pressure dependence coefficient (n)	0.5				0.5
Contraction parameter (c_1)	0.107	0.07	0.05	0.01	0.07
Dilation parameter (d_1)	0	0	0.06	0.06	0.06
Maximum Shear Strain (γ_{max})	0.1	0.1	0.1	0.1	0.1
Reference mean confinement p'_r (kPa)	101				101
Permeability (m/s)	1×10^{-5}	1×10^{-6}	1×10^{-4}	1×10^{-6}	5×10^{-5}
Initial Stiffness Proportional damping (ξ)	0.003				0.003
Convergence criteria based on norm of energy increment	1×10^{-7}				1×10^{-7}

(i) Offshore site   (ii) Nearshore site
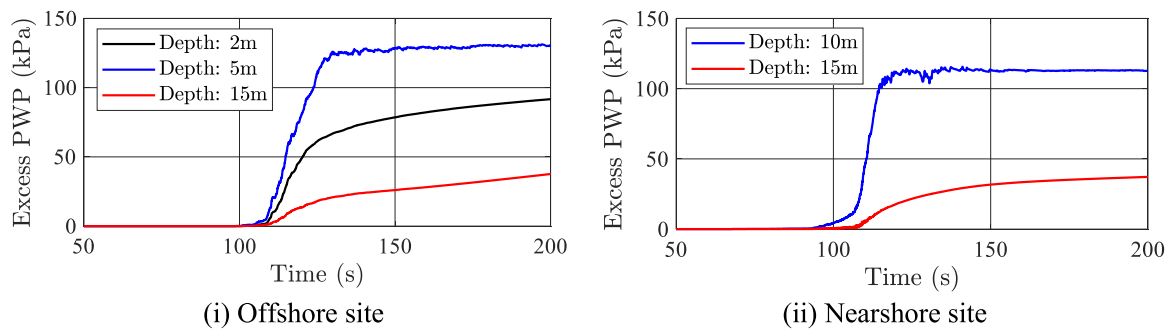
Fig. 14. Computed excess pore pressure response. (i) Kamisu offshore wind farm (ii) Kamisu nearshore wind farm

(i) Offshore site   (ii) Nearshore site
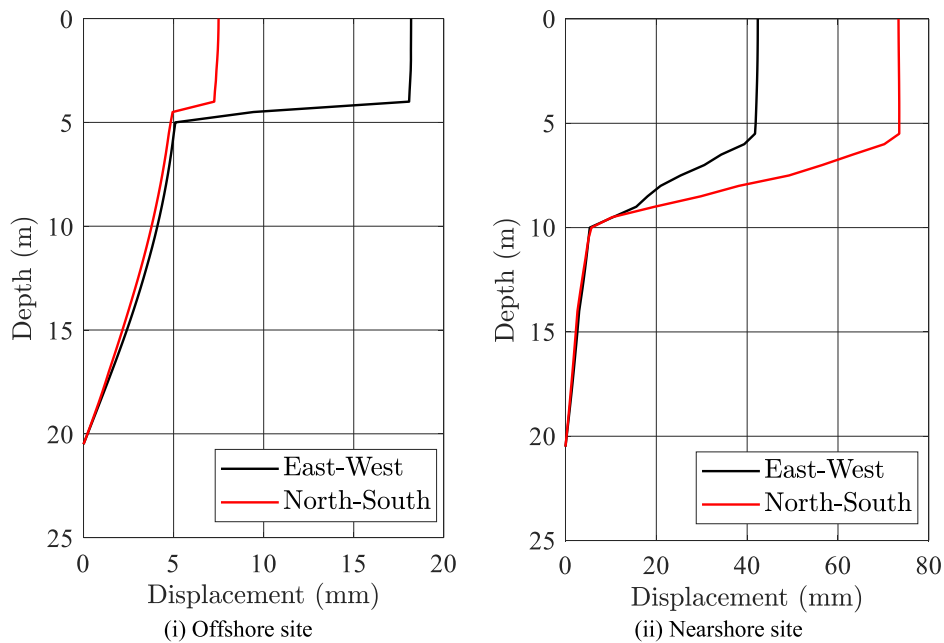
Fig. 15. Displacement response of the ground: (i) Offshore wind farm (ii) Nearshore wind farm.

Table 3
Load cases considered for the Kamisu offshore wind farm.

Design load case (DLC)	Description	Load configuration
A	Extreme Wind + Wave	985 KN + 168 kN/m (6.92 m from the mudline level)
B	Operating Wind + Wave	293 KN + 138 kN/m (10.2 m from the mudline level)
C	Static Wind + Tsunami	190 KN + 138 kN/m (10.2 m from the mudline level)
D	Extreme Wind + Wave + Earthquake load	985 KN + 168 kN/m + Earthquake displacement demand

Table 4
Load cases considered for the Kamisu nearshore wind farm.

Design load case (DLC)	Description	Load configuration
E	Extreme Wind	985 KN
F	Static Wind + Tsunami (Including soil liquefaction)	190 KN + 138 kN/m Earthquake displacement demand (5 m from the mudline level)
G	Extreme Wind + Earthquake load (Including soil liquefaction)	985 KN + Earthquake displacement demand

The configurations for the nearshore turbines are presented in Fig. 17 (i) and (iii). Similarly, Fig. 17 (ii) and (iv) illustrate the configuration of the offshore turbines.

Soil-pile interaction was modeled through nonlinear springs at regular intervals. Since only the lateral pile response is studied, soil springs are provided only in the two horizontal directions (i.e., earthquake motion direction). In both models, API p-y curves [56] and hyperelastic p-y springs proposed by Dash et al. [27] were used to model the non-liquefiable layers were used to model the liquefiable layers.

The wind turbine structure was modeled at the top of a monopile foundation, and aerodynamic mass dampers (bi-directional) were assigned at the top of the tower. The assigned aerodynamic damper parameters were found using Adhikari and Bhattacharya [57]. Translational and rotational inertia of the RNA is assigned at the top of the tower. Mass distribution of the tower is explicitly modeled through point masses specified along the tower length. The selection of appropriate damping is critical for the design and analysis of OWTs [5]. In this analysis, Rayleigh damping was considered. The damping ratio for the structural analysis of the wind turbine is varied between 1% and 20% [57,58] to understand the effect of damping factor variation on the design requirements.

The turbine structure and foundation specifications are provided in Table 5.

The fixed base frequency of the tower is estimated as 0.43 Hz, similar to the value provided in Ref. [42]. The natural frequency of the tower-foundation system of offshore wind turbines under pre and post-liquefaction conditions are estimated as 0.38 Hz and 0.36 Hz,

(i) Discretization   (ii) Wave Loading   (iii) Tsunami Loading
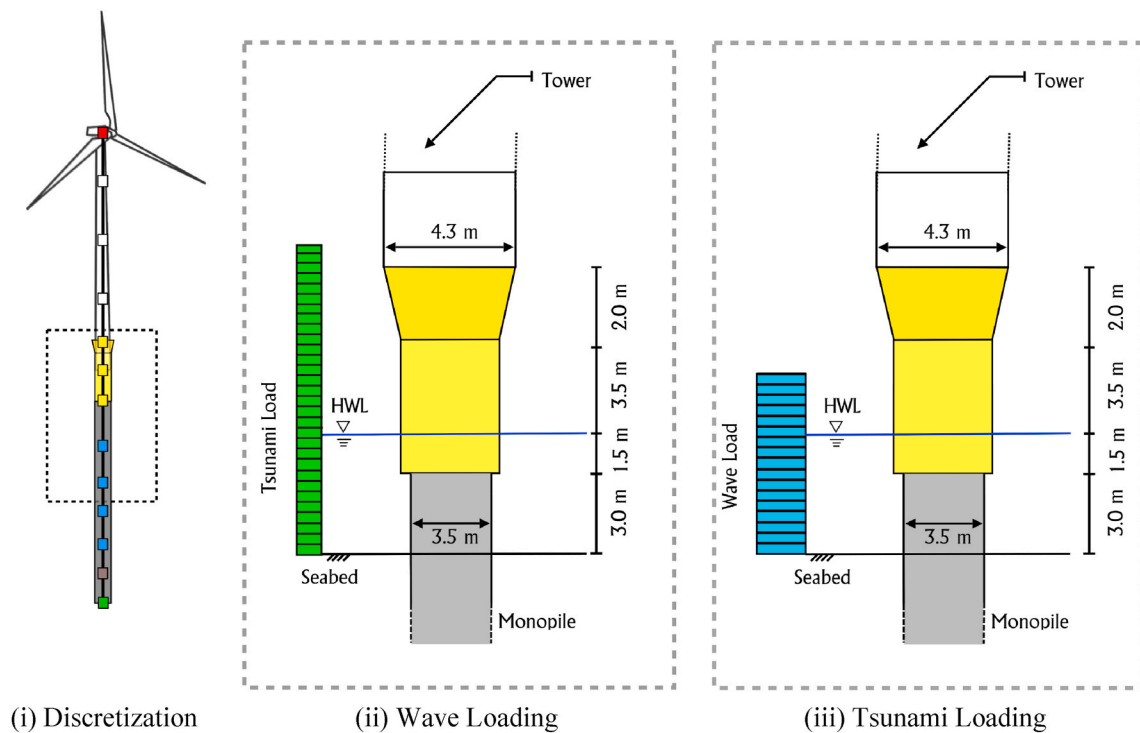
Fig. 16. Load distribution profiles on offshore turbine due to (ii) Wave and (iii) Tsunami loading.
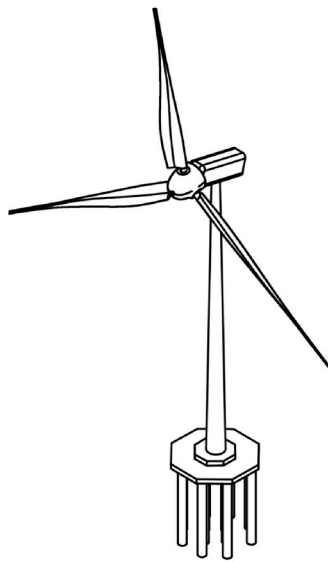
(i) Nearshore Turbine: Isometric View
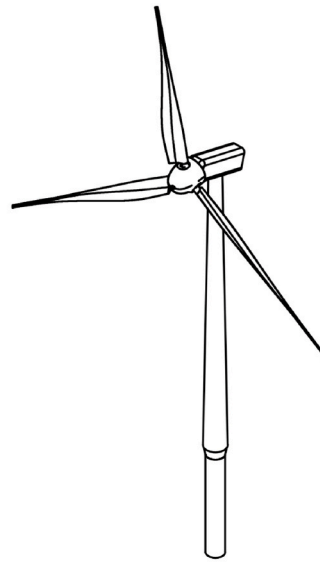
(ii) Offshore Turbine: Isometric View
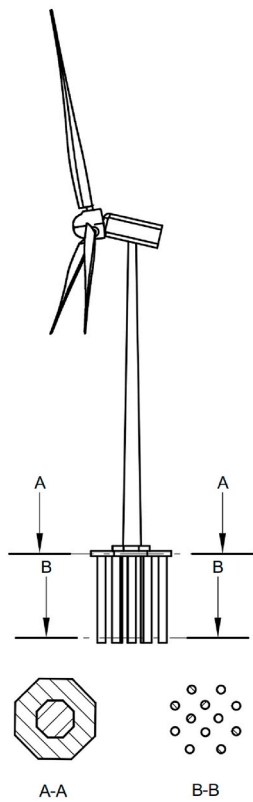
(iii)Nearshore Turbine: Cross Section
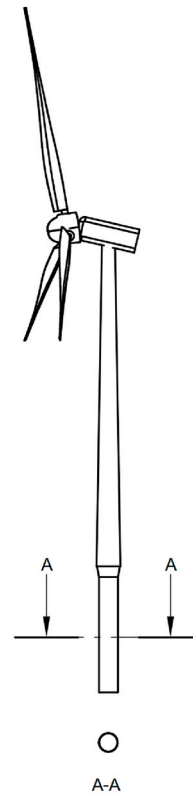
(iv)Offshore Turbine: Cross Section

Fig. 17. Typical configuration of Kamisu nearshore wind farm.

Table 5

Turbines and foundation specifications [10,42,59].

Kamisu offshore wind farm		Kamisu nearshore wind farm	
Turbine model	Hitachi 2.0–80	Turbine model	Subaru 2.0–80
Hub height [m]	60	Hub height [m]	60
Pile length [m]	17	Pile length [m]	17
Equivalent top mass [tons]	108	Equivalent top mass [tons]	108
Blade length [m]	80	Blade length [m]	80
Blade weight [tons]	6.7	Blade weight [tons]	6.7
Tower top & bottom diameter [m]	1.5–4.3	Tower top & bottom diameter [m]	1.5–4.3
Diameter of the transition piece [m]	3.8–4.35	Number of piles	12
Tower thickness average [mm]	15	Tower thickness average [mm]	15
Pile diameter [m]	3.5	Pile diameter [m]	0.8
Pile thickness [m]	0.042	Pile thickness [m]	0.3
Tower thickness average [mm]	15	Diameter of pile cap [m]	13
Thickness of the transition piece [mm]	20	Pile cap stiffness	rigid
Plastic Moment Capacity [MNm] of monopile	177.5	Plastic Moment Capacity [MNm] of a single pile	29.8

respectively. These values for nearshore wind turbines are estimated as 0.37 Hz and 0.36 Hz. Table 6 and Table 7 describes key outputs from the back analysis.

Results show that the monopile-supported offshore turbine remained safe for all load cases analyzed (Fig. 18). Further, pile head rotation and tilt were found to satisfy the prescribed performance objectives. In contrast, the analysis indicated limit state exceedance (for pile head rotation) in the pile group supported nearshore turbine. The RNA acceleration for offshore and nearshore turbines indicated sensitivity to the employed damping ratio (ξ%).

Fig. 18 (i) and Fig. 18 (ii) present the normalized moment profiles (for load cases presented earlier) for the piles normalized with the plastic moment capacity (177.5 MNm and 29.8 MNm) of offshore and nearshore wind farms. The ratio between the maximum observed moment due to the applied loading and the plastic moment capacity (M/M_p) was approximately 0.47 and 0.85 for offshore and nearshore wind turbines. These maximum bending moment values were observed for seismic load cases (D and G) for offshore and nearshore sites.

Matsunobu et al. [42] studied Kamisu offshore wind farms, assuming

Table 7

Natural frequency (f_1), pile head displacement (Δ), pile head rotation (θ), RNA acceleration (a_{RNA}), and maximum bending moment (M_{max}) on a single pile in the pile group: Nearshore.

Load case	(ξ%)	f_1 (Hz)	Δ_{max} [$\Delta_{residual}$] (mm)	θ_{max} [$\theta_{residual}$] (deg)	a_{RNA} (g)	M_{max} (MNm)
E	N/A	0.37	0.10	0.01	N/A	3.0
F	N/A	0.36	0.05	0.005	N/A	2.6
G (1-6)	1	0.36	189.00 [22.4]	1.49 [0.17]	0.14	25.5
	2		188.60 [22.4]	1.49 [0.17]	0.13	25.5
	4		187.80 [22.4]	1.49 [0.17]	0.11	25.4
	8		187.40 [22.4]	1.49 [0.17]	0.09	25.4
	12		186.40 [22.4]	1.47 [0.17]	0.08	25.3
	20		182.50 [22.4]	1.43 [0.17]	0.07	25.1

a fixed base and nonphysical properties for the ground. The obtained bending values found by Matsunobu et al. [42] ranges between 20 and 65 MNm, whereas this paper found a range between 19.2 and 83.9 MNm at the mud-line level for considered load cases.

3.4. Load utilization ratio

The demand to capacity ratio of the monopile under combined lateral and flexural loading is obtained through a load utilization ratio. In this study, for each design load case (DLC), the demand is presented and compared to the system capacity, as shown in Fig. 19 and Fig. 20. The capacity (yield surface) is estimated using OPILE [60] and using API [56] p-y curves for the pre-liquefaction and the hyperelastic p-y curves [26,27] with residual shear strength based on Stark and Mesri [61], for the post liquefaction condition. The ultimate capacity of soil for the lateral load (H_R) and then the ultimate capacity of soil for moment load (M_R) was obtained. These two points (M_R, H_R) were connected using a line to define a simplified failure envelope for simplification.

Results summarized in Figs. 19 and 20 indicate that the back analysis indicated that the design load cases are below the failure surface for offshore and nearshore turbines, respectively. The DLCs were found to satisfy each limit state. The results show that the offshore wind turbine DLCs were at least 3.44 times away from the failure envelope in the worst-case scenario (Post liquefaction). Also, this value was found to be at least 1.57 times away from the failure envelope for the nearshore wind turbines.

The analysis predicts that the monopile (for the offshore turbines)

Table 6

Natural frequency (f_1), pile head displacement (Δ), pile head rotation (θ), RNA acceleration (a_{RNA}), and maximum bending moment (M_{max}) on the monopile: Offshore.

Load case	(ξ%)	f_1 (Hz)	Δ_{max} [$\Delta_{residual}$] (mm)	θ_{max} [$\theta_{residual}$] (deg)	a_{RNA} (g)	M_{max} (MNm)
A	N/A	0.38	43.00	0.39	N/A	76.0
B	N/A	0.38	15.00	0.14	N/A	28.5
C	N/A	0.36	9.00	0.07	N/A	19.2
D (1–6)	1	0.36	74.60 [51.0]	0.45 [0.41]	0.06	83.9
	2		73.20 [51.0]	0.44 [0.41]	0.05	83.5
	4		72.50 [51.0]	0.43 [0.41]	0.04	82.8
	8		72.10 [51.0]	0.43 [0.41]	0.04	82.0
	12		72.00 [51.0]	0.43 [0.41]	0.03	81.5
	20		71.80 [51.0]	0.43 [0.41]	0.03	80.9

(i) Induced moments for monopile in Offshore Turbine

(ii) Induced moments for a single pile in pile group for the nearshore Turbine

Fig. 18. Bending moment diagrams of a turbine for Offshore and Nearshore Kamisu wind farm.
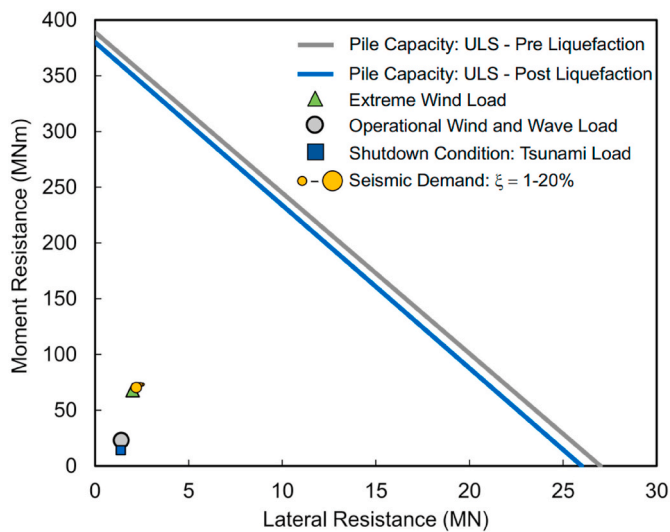
Fig. 19. Example load utilization diagram of Kamisu offshore wind farm.
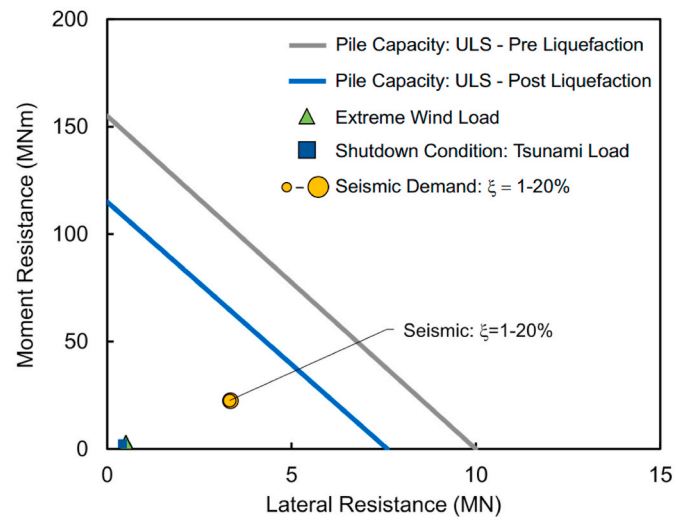
Fig. 20. Example load utilization diagram of Kamisu nearshore wind farm.

should remain within the failure surface envelope and therefore not develop plastic response. Based on field observations from Bhattacharya and Goda [45], the foundation remained safe and resumed its operation after inspection.

Further, the analysis indicated vulnerability of the nearshore turbine to liquefaction-induced ground deformations. Post-earthquake reconnaissance surveys indicated that all but one (due to extensive tilt) of the turbines were functional post strong shaking. Therefore, it is likely that the spatial variability of the deposit played a significant role in the performance of the tilted turbine. Some evidence of the effect of spatial variability is visible in Fig. 9 (i), where preferential manifestation of soil ejecta is observed towards the north of the turbine (direction of observed tilt), which may have contributed to the response.

Tables 8 and 9 present full details of the load utilization ratios (R/A) for the different load cases.

Table 8
Load utilization ratio for the offshore wind farm.

Load cases	DLCs			Resistance Capacity		
	H_i (MN)	M_i (MNm)		H_R (MN)	M_R (MNm)	R/A
A	2.00	68.00		27.00	389.00	4.02
B	1.40	23.00				9.01
C	1.37	14.14		26.00	380.00	11.12
D.1 ($\xi = 1\%$)	2.54	73.20				3.44
D.2 ($\xi = 2\%$)	2.43	72.70				3.51
D.3 ($\xi = 4\%$)	2.33	72.00				3.58
D.4 ($\xi = 8\%$)	2.26	71.20				3.65
D.5 ($\xi = 12\%$)	2.23	70.80				3.68
D.6 ($\xi = 20\%$)	2.20	70.30				3.71

Table 9
Load utilization ratio for the nearshore wind farm.

Load cases	DLCs		Resistance Capacity		
	H_i (MN)	M_i (MNm)	H_R (MN)	M_R (MNm)	R/A
E	0.51	2.97	10.00	155.00	37.70
F	0.41	2.49	7.60	115.00	44.80
G (ξ = 1%)	3.28	22.69			1.59
G (ξ = 2%)	3.29	22.66			1.59
G (ξ = 4%)	3.29	22.61			1.59
G (ξ = 8%)	3.30	22.58			1.58
G (ξ = 12%)	3.32	22.57			1.58
G (ξ = 20%)	3.35	22.33			1.57

3.5. Soil settlement at Kamisu wind farm

Estimation of soil settlement at the nearshore and offshore sites was assessed based on the stratigraphy shown in Fig. 21. The triggering analysis was carried out based on Idriss and Boulanger [28], and estimates of the consolidation-induced settlement were obtained from Ishihara and Yoshimine [37]. The analysis predicted initial liquefaction between depths of 5–10 m and 0–4 m for the onshore and offshore sites. Estimated post liquefaction consolidation settlements were generally about 0.15–0.2 m for the nearshore and offshore sites corroborating well with land subsidence reconnaissance surveys [62] which estimate soil settlement of about 0.15 m in the Ibaraki region.

Photographic evidence (Fig. 10, ii) in proximity to the nearshore turbines indicate that soil had settled around the pile group, leading to the observed vertical fissures near the top of the pile cap. Therefore, it is likely that the sufficient end-bearing resistance of the nearshore pile group prevented the settlement of the OWT.

4. Discussion and conclusions

An existing framework for the foundation design of monopile-supported wind turbines was extended to include seismic load considerations in liquefiable and non-liquefiable soil. The framework was validated using a case study from Wind Power Kamisu, a near-shore farm that performed well during the 2011 Tohoku earthquake and subsequent tsunami.

The discussion and conclusions are presented succinctly below:

1. A quantitative appraisal of appropriate damping, as recommended by Lombardi and Bhattacharya [58] and Adhikari and Bhattacharya [57], could vary the structural demands and therefore needs proper consideration. Back analysis of a case study from the Kamisu wind farm further indicated that structural demands could vary if suitable damping models are not selected.
2. Definition of mechanism-specific *p-y* spring models for liquefiable and non-liquefiable soil is necessary as their selection could underpredict or overpredict structural response (deformation, tilt, RNA acceleration). As near-level ground conditions prevailed in this study, the authors employed hyperelastic (strain hardening) *p-y* curves for liquefiable soil to account for the increased resistance attributed to shear strain-induced soil dilation. During shear strain excursions, such dilative tendencies can transfer high acceleration pulses to the RNA and therefore need to be accounted for in the design stage.
3. Load utilization ratio (R/A) type analyses can be conducted to ensure that design load cases are within the failure envelope. Multiple constitutive models can be used to estimate the failure surface to handle epistemic uncertainties. Such a representation allows for a simple graphical way to estimate the conservatism required in design.
4. Using the proposed framework, back analysis of a set of turbines from an offshore and near-shore wind farm (Wind Power Kamisu)

(i) Kamisu nearshore wind farm　　　(ii) Kamisu offshore wind farm
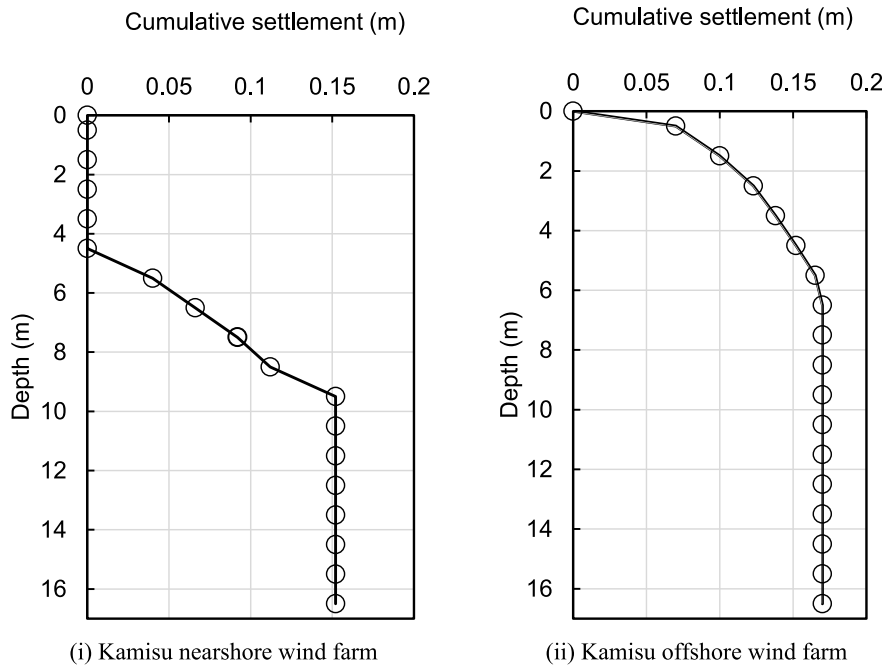
Fig. 21. Cumulative settlement of Kamisu wind farms during Tohoku 2011 earthquake (i) Nearshore site (ii) Offshore site.

during the 2011 Tohoku earthquake and subsequent tsunami indicated its sufficiency. The analysis was able to contrast the good overall performance of the offshore turbines and the limit state exceedance of the nearshore turbines.

References

[1] IRENA. Renewable capacity statistics. Abu Dhabi. 2021.
[2] Kaynia AM. Seismic considerations in design of offshore wind turbines. Soil Dynam Earthq Eng 2019;124:399–407. https://doi.org/10.1016/j.soildyn.2018.04.038.
[3] Li X, Zeng X, Yu X, Wang X. Seismic response of a novel hybrid foundation for offshore wind turbine by geotechnical centrifuge modeling. Renew Energy 2021; 172:1404–16. https://doi.org/10.1016/j.renene.2020.11.140.
[4] Wang X, Yang X, Zeng X. Seismic centrifuge modelling of suction bucket foundation for offshore wind turbine. Renew Energy 2017;114:1013–22. https:// doi.org/10.1016/j.renene.2017.07.103.
[5] Ko YY. A simplified structural model for monopile-supported offshore wind turbines with tapered towers. Renew Energy 2020;156:777–90. https://doi.org/ 10.1016/j.renene.2020.03.149.
[6] Elgamal A, Yang Z, Parra E, Ragheb A. Modeling of cyclic mobility in saturated cohesionless soils. Int J Plast 2003;19:883–905. https://doi.org/10.1016/S0749-6419(02)00010-4.
[7] Wang X, Zeng X, Li X, Li J. Liquefaction characteristics of offshore wind turbine with hybrid monopile foundation via centrifuge modelling. Renew Energy 2020; 145:2358–72. https://doi.org/10.1016/j.renene.2019.07.106.
[8] Mo R, Cao R, Liu M, Li M. Effect of ground motion directionality on seismic dynamic responses of monopile offshore wind turbines. Renew Energy 2021;175: 179–99. https://doi.org/10.1016/j.renene.2021.05.036.
[9] Zayed M, Kim K, Elgamal A. Shake table testing for suction bucket foundation wind turbine seismic response. Honolulu, Hawaii, USA: 29th Int. Ocean Polar Eng. Conf.; 2019. p. 2111–6.
[10] 4coffshore. Wind Turbine Information Database; 2021. https://www.4coffshore.com/windfarms/turbines.aspx. [Accessed 5 May 2021].
[11] Bhattacharya S. Design of foundations for offshore wind turbines. In: Wiley, editor. First Edit. Chichester; 2019. https://doi.org/10.1002/9781119128137.
[12] Arany L, Bhattacharya S, Macdonald J, Hogan S. Design of monopiles for offshore wind turbines in 10 steps. Soil Dynam Earthq Eng 2017;92:126–52. https://doi.org/10.1016/j.soildyn.2016.09.024.
[13] Yoshida N. Engineering seismic base layer for defining design earthquake motion. AIP Conf Proc 2008;1020:346–53. https://doi.org/10.1063/1.2963855.
[14] Santini A, Moraci N. 2008 seismic engineering conference commemorating the 1908 Messina and Reggio calabria eartquake : [(MERCEA '08]; Reggio calabria, Italy, 8 - 11 July 2008/ed. Adolfo Santini. Pt. 1. AIP Conf. Proc. 2008;1020(1). Melville, NY: American Inst. of Physics.
[15] Nikolaou S, Mylonakis G, Gazetas G, Tazoh T. Kinematic pile bending during earthquakes: analysis and field measurements. Géotechnique 2001;51:425–40. https://doi.org/10.1680/geot.2001.51.5.425.
[16] Tokimatsu K, Asaka Y. Effects of liquefaction-induced ground displacements on pile performance in the 1995 hyogoken-nambu earthquake. Soils Found 1998;38: 163–77. https://doi.org/10.3208/sandf.38.special_163.

[17] Baker JW. Conditional mean spectrum: tool for ground-motion selection. J Struct Eng 2011;137:322–31. https://doi.org/10.1061/(ASCE)ST.1943-541X.0000215.
[18] Kwong NS, Chopra AK. A generalized conditional mean spectrum and its application for intensity-based assessments of seismic demands. Earthq Spectra 2017;33:123–43. https://doi.org/10.1193/040416eqs050m.
[19] Katsanos EI, Sextos AG, Manolis GD. Selection of earthquake ground motion records: a state-of-the-art review from a structural engineering perspective. Soil Dynam Earthq Eng 2010;30:157–69. https://doi.org/10.1016/j.soildyn.2009.10.005.
[20] Idriss IM. Earthquake ground motions at Soft soil sites. Int. Conf. Recent adv. Geotech. Earthq. Eng. Soil dyn. St. Louis, Missouri: University of Missouri-Rolla 1991;3:2265–75.
[21] Kramer SL. Geotechnical earthquake engineering. first ed. Prentice Hall; 1996.
[22] Idriss I, Sun JI. SHAKE91: a computer program for conducting equivalent linear seismic response analyses of horizontally layered soil deposits. Davis Calif: Department of Civil and Environmental Engineering; 1992. Center for Geotechnical Modeling Dept. of Civil and Environmental Engineering University of California Davis.
[23] Boulanger RW, Kutter BL, Brandenberg SJ, Singh P, Chang D. Pile foundations in liquefied and laterally spreading ground during earthquakes: centrifuge experiments & analyses. Davis, California. 2003.
[24] Franke KW, Rollins KM. Simplified hybrid p-y spring model for liquefied soils. J Geotech Geoenviron Eng 2013;139:564–76. https://doi.org/10.1061/(ASCE) GT.1943-5606.0000750.
[25] Railway Technical Research Institute (RTRI). Design standard for railway facilities-seismic design-Japan. Japan. 1999.
[26] Lombardi D, Dash SR, Bhattacharya S, Ibraim E, Muir Wood D, Taylor CA. Construction of simplified design p – y curves for liquefied soils. Géotechnique 2017;67:216–27. https://doi.org/10.1680/jgeot.15. .116.
[27] Dash S, Rouholamin M, Lombardi D, Bhattacharya S. A practical method for construction of p-y curves for liquefiable soils. Soil Dynam Earthq Eng 2017;97: 478–81. https://doi.org/10.1016/j.soildyn.2017.03.002.
[28] Idriss IM, Boulanger RW, Institute. EER. Soil liquefaction during earthquakes. second ed. Oakland, Calif: Earthquake Engineering Research Institute; 2008.
[29] Robertson PK, Wride (Fear) CE. Evaluating cyclic liquefaction potential using the cone penetration test. Can Geotech J 1998;35(3):442–59. https://doi.org/10.1139/t98-017.
[30] Kayen R, Moss RES, Thompson EM, Seed RB, Cetin KO, Kiureghian A Der, et al. Shear-wave velocity–based probabilistic and deterministic assessment of seismic soil liquefaction potential. J Geotech Geoenviron Eng 2013;139:407–19. https://doi.org/10.1061/(ASCE)GT.1943-5606.0000743.
[31] Seed RB, Cetin KO, Kammerer AM, Wu J, Pestana JM, Riemer MF, et al. Recent advances in soil liquefaction engineering: a unified and consistent framework. California: 26th Annu. ASCE Los Angeles Geotech. Spring Semin.; 2003.
[32] Beyzaei CZ, Bray JD, Cubrinovski M, Bastin S, Stringer M, Jacka M, et al. Characterization of silty soil thin layering and groundwater conditions for liquefaction assessment. Can Geotech J 2020;57:263–76. https://doi.org/10.1139/cgj-2018-0287.
[33] Aleem M, Emre Demerici H, Bhattacharya S, Demirci HE, Bhattacharya S, Kingdom U. Lateral and moment resisting capacity of monopiles in layered soils. Kayseri, Turkey: ICEESEN 2020; 2020. p. 19–21.
[34] Aleem M, Bhattacharya S, Cui L, Amani S, Salem AR, Jalbi S. Load utilisation (LU) ratio of monopiles supporting offshore wind turbines: formulation and examples from European Wind Farms. Ocean Eng 2022;248:110798. https://doi.org/10.1016/j.oceaneng.2022.110798.
[35] Lee D-H, Ku C-S, Juang CH. Soil liquefaction and ground settlement in chi-chi taiwan. Earthquake. Int. Conf. Recent Adv. Geotech. Earthq. Eng. Soil Dyn. 2001: 27.
[36] Tokimatsu K, Seed HB. Evaluation of settlements in sands due to earthquake shaking. J Geotech Eng 1987;113:861–78. 10.1061/ASCE)0733-9410(1987)113:8 (861.
[37] Ishihara K, Yoshimine M. Evaluation of settlements in sand deposits following liquefaction during earthquakes. Soils Found 1992;32:173–88. https://doi.org/10.3208/sandf1972.32.173.
[38] Zhang G, Robertson PK, Brachman RW. Estimating liquefaction-induced ground settlements from CPT for level ground. Can Geotech J 2002;39:1168–80. https://doi.org/10.1139/t02-047.
[39] Ashford SA, Boulanger RW, Donahue JL, Stewart JP, Harder Jr LF, Kik, et al. GEER reconnaissance reports. 2011.
[40] Google Earth Pro. Condition of Kamisu nearshore wind farm 18 days after Tohoku 2011 earthquake [471625m E, 3979757m N. 2011.
[41] Tsukamoto Y, Kawabe S, Kokusho T. Soil liquefaction observed at the lower stream of tonegawa river during the 2011 off the pacific coast of Tohoku earthquake. Soils Found 2012;52:987–99. https://doi.org/10.1016/j.sandf.2012.11.016.
[42] Matsunobu Takashi, Inoue Shinzo, Tsuji Yoshiyuki, Yoshida Kenji, Komatsuzaki Mamoru. Seismic design of offshore wind turbine withstands Great East Japan earthquake and tsunami. J Energy Power Eng 2014;8:2039–44. https://doi.org/10.17265/1934-8975/2014.12.007.
[43] National Research Institute for Earth Science and Disaster Resilience. NIED K-NET, KiK-net 2019.
[44] Fraser S, Raby A, Pomonis A, Goda K, Chian SC, Macabuag J, et al. Tsunami damage to coastal defences and buildings in the March 11th 2011 M w 9.0 Great East Japan earthquake and tsunami. Bull Earthq Eng 2013;11:205–39. https://doi.org/10.1007/s10518-012-9348-9.

[45] Bhattacharya S, Goda K. Use of offshore wind farms to increase seismic resilience of Nuclear Power Plants. Soil Dynam Earthq Eng 2016;80:65–8. https://doi.org/10.1016/j.soildyn.2015.10.001.

[46] Prideaux E. The wind farm that withstood the Japanese tsunami. Haymarket Media Gr Ltd; 2011. https://www.windpowermonthly.com/article/1061942/wind-farm-withstood-japanese-tsunami. [Accessed 21 October 2021].

[47] JFS – Japan for Sustainability. Offshore wind farm withstands Great East Japan earthquake and tsunami. JFS Japan for Sustainability; 2011. www.japanfs.org/en/news/archives/news_id031055.html.

[48] Google Earth Online. 9338908,140.71678348. Location of Kamisu wind farm, vol. 35; 2021. https://earth.google.com/web/search/kamisu/@35.9338908. [Accessed 16 April 2021]. ,140.71678348,-8.00856191a ,50400.57018575d,35y,-0h,0t,0r/data=CigiJgokCZzMVJssuDdAEZvMVJssu DfAGWO6LkxgWERAIblM3NJHb1DA.

[49] Commons Wikimedia. Wind power stations(wind power Kamisu). 2017. https://commons.wikimedia.org/wiki/File:Wind_Power_Kamisu_10.jpg. [Accessed 16 April 2021].

[50] Hashash YMA, Musgrove MI, Harmon JA, Ilhan O, Xing G, Numanoglu O, et al. DEEPSOIL V7.0, user manual. Urbana, IL: Board of Trustees of University of Illinois at Urbana-Champaign; 2020.

[51] Anbazhagan P, Prabhakaran A, Madhura H, Moustafa SSR, Al-Arifi NSN. Selection of representative shear modulus reduction and damping curves for rock, gravel and sand sites from the KiK-Net downhole array. Nat Hazards 2017;88:1741–68. https://doi.org/10.1007/s11069-017-2944-x.

[52] NIED. Geo-Station 2016. https://www.geo-stn.bosai.go.jp/mapping_page.html. [Accessed 21 October 2021].

[53] Elgamal A, Yang Z, Lu J. Cyclic1D: a computer program for seismic ground response. Report No. SSRP-06/05. San Diego. 2006.

[54] Yang Z, Elgamal A, Parra E. Computational model for cyclic mobility and associated shear deformation. J Geotech Geoenviron Eng 2003;129:1119–27. 10.1061/ASCE)1090-0241(2003)129:12(1119.

[55] Global wind Atlas version 3.0. Global Wind Atlas; 2018. https://globalwindatlas.info. [Accessed 1 January 2018]. accessed.

[56] API. Recommended practice for planning, designing and constructing fixed offshore platforms- working stress design. API Recomm Pract 2007;24:242. WSD.

[57] Adhikari S, Bhattacharya S. A general frequency adaptive framework for damped response analysis of wind turbines. Soil Dynam Earthq Eng 2021;143:106605. https://doi.org/10.1016/j.soildyn.2021.106605.

[58] Lombardi D, Bhattacharya S. Modal analysis of pile-supported structures during seismic liquefaction. Earthq Eng Struct Dynam 2014;43:119–38. https://doi.org/10.1002/eqe.2336.

[59] Tottori Prefectural Government. List of domestic offshore wind power generation. 2013. https://www.pref.tottori.lg.jp/secure/836760/siryou6-2-1.pdf. [Accessed 10 June 2021]. accessed.

[60] Cathie Associates. OPILE, Integrated solutions for single pile analysis : instruction Manual. 2015.

[61] Stark TD, Mesri G. Undrained shear strength of liquefied sands for stability analysis. J Geotech Eng 1992;118:1727–47. 10.1061/ASCE)0733-9410(1992)118:11(1727.

[62] Imakiire T, Koarai M. Wide-area land subsidence caused by "the 2011 off the pacific coast of Tohoku earthquake. Soils Found 2012;52:842–55. https://doi.org/10.1016/j.sandf.2012.11.007.